Int. J. Electrochem. Sci., 9 **(2014)** 46 - 60

International Journal of
ELECTROCHEMICAL
SCIENCE
www.electrochemsci.org

A Facile Route to Controllable Synthesis of Fe_3O_4/Graphene Composites and Their Application in Lithium-Ion Batteries

Changjing Fu[*], *Guogang Zhao*[*], *Haijun Zhang*, *Shuang Li*

Engineering Institute of Graphite New Materials, Heilongjiang University of Science and Technology, 2468 Puyuan Road, Harbin 150022, P.R. China
[*]E-mail: fcj_hit@163.com, zgg1963@126.com

Received: 22 August 2013 / *Accepted:* 9 October 2013 / *Published:* 15 November 2013

A facile and straightforward method has been developed to synthesize laminated-structured Fe_3O_4/graphene composite through solvothermal reaction. The particle size and coverage density of Fe_3O_4 on graphene sheets were controlled by adjusting the molar ratio of graphite oxide (GO) and Fe (II) ions. Spherical Fe_3O_4 nanoparticles were decorated densely and homogeneously on the graphene sheets. Galvanostatic charge-discharge cycling of the optimized Fe_3O_4/graphene composite exhibited a reversible specific capacity more than 963 mAh g^{-1} after 100 cycles without detectable capacity fading at the current density of 100 mA g^{-1}. Even after 50 cycles at various rates from 100 to 2500 mA g^{-1}, it still maintained the specific capacity of 979 mAh g^{-1} at 100 mA g^{-1}. The highly improved performance of Fe_3O_4/graphene composite could be attributed to the pinning effect of hydroxyl/epoxy groups on Fe atoms of Fe_3O_4 nanoparticles and the excellent interfacial interaction between Fe_3O_4 and graphene.

Keywords: Graphene, Fe_3O_4, Controllable synthesis, Lithium-ion battery, Anode

1. INTRODUCTION

Rechargeable lithium-ion batteries (LIBs) have long been considered as an attractive power sources for a wide variety of applications over traditional rechargeable battery systems [1, 2]. Especially in recent years, with the development of electrical/hybrid vehicles, LIBs are expected to be the most promising power sources [3]. To further improve the capacity and energy density of the battery system, much effort has been focused on the researches of high-performance electrodes for next-generation LIBs [4]. The breakthrough for LIBs anodes, gained by Tarascon et al. in 2000, was the development of transition metal oxides as anode materials, which exhibited a much higher theoretical specific capacity than that of the traditional graphite electrodes [5]. But, regretfully, these oxides showed poorer cycling stability and lower coulomb efficiency due to their volume or chemical

changes and particle aggregation during the charge-discharge process [6]. Numerous efforts have been made to combine oxides with various carbons to form a hybrid structure to overcome the shortcomings of oxides [7]. Graphene has attracted increasing interest because of their amazing properties, such as excellent electrical conductivity, high surface area, and ultra thin planar structure, so that it is believed to be a potential electrode material [8, 9]. However, due to the van der waals interactions, which induces to the irreversible agglomerates or restack of the unfunctionalized graphene sheets to form graphite, graphene-based materials as anode materials of LIBs suffer from a large irreversible capacity, low initial Coulombic efficiency, and fast capacity fade despite a large initial discharge capacity [10]. Therefore, study on graphene-based composites should be focused on the reduction of the restacking and on the improvement of the stabilization [11].

Graphene-metal oxide composites are good candidates as anode materials of LIBs [12]. Some metal oxide-graphene composites have been fabricated in order to investigate their Li-ion storage properties and to improve LIBs' cycling performance and rate capacities [13]. As a matrix of metal oxide nanoparticles, graphene could not only effectively improve the mechanical stability and electrochemical performance of LIBs, but also provides some novel physical and chemical properties which couldn't be obtained from graphene or metal oxide itself [14].

Among the transition metal oxides, iron oxides have attracted much attention due to their abundant, inexpensive and environmentally friendly. More importantly, it has a relatively high theoretical Li storage capacity, which suggests that iron oxides may offer high pseudo charge capacitance through redox reduction [15]. Unfortunately, the practical application of iron oxides in LIBs is also strongly restricted by their low conductance and inferior cycling stability during Li^+ insertion/extraction processes [16]. The fantastic properties of iron oxides/graphene nanohybrids as anode active materials of LIBs have already been discovered and many published papers have demonstrated that modifying iron oxides with graphene is an effective method to improve their properties for LIBs [17]. However, a suitable ratio of iron oxides to graphene is of paramount importance, which gives the optimized coverage of nanoparticles and ensures the integration of both the high capacity of the transition metal oxides and the excellent cycling stability of the improved graphene sheets [18]. A huge amount of iron oxides nanoparticles covering the surface of graphene sheets will cause the overlap of the superfluous nanaparticals, thus a large quantity of iron oxides nanoparticles will lose direct contact with graphene, leading to a poor electric conductivity of the composite. On the contrary, a fewer amount of iron oxides covering will result in a bad volume buffering effect [19]. It is, thus, essential to homogeneously anchor the individual iron oxides nanoparticles on graphene. The ratio between the graphene and the metal oxides should be tuned to enhance the electrochemical performance of the composite. However, the reported synthesis methods always need surfactants or highly viscous solvents to avoid the aggregation of the final nanoparticles. The introduction of these additional additives inevitably makes the solid-liquid separation more complex. Therefore, it is still a challenge for iron oxides nanoparticles to be well adhered and homogeneously distributed on the surface of graphene.

In this article, Fe_3O_4/graphene composites were synthesized through a facile solvothermal process, in which the formation of Fe_3O_4 nanoparticles, the reduction of GO, and the uniform mixing of these two materials were accomplished in one step. The solvent of ethanol also played the role of

reduction media during the synthesis. Ethanol-assisted reduction method effectively avoided the shortcomings of other traditional reduction processes. Moreover, the graphene and Fe_3O_4 nanohybrids were synthesized in a controlled molar ratio. The interactions between each oxygen-containing functional group and Fe_3O_4 were analyzed in detail. The effects of the molar ratio between graphene and Fe_3O_4 on the anodes' performance of LIBs were also studied. This work revealed the important factors affecting the high-rate performance and cyclic stability of Fe_3O_4/graphene composites, and provided an effective way to the controllable synthesis of the anode materials based on graphene nanosheets for LIBs.

2. EXPERIMENTAL

2.1 Preparation of Fe_3O_4/graphene composites

All of the reagents were of analytical grade and were used without further purification. Distilled water was used in all experiments. Graphite oxide (GO) was prepared from natural graphite powder according to the modified Hummer's method [20]. Exfoliation was carried out by sonicating GO in ethanol to form a homogeneous dispersion (1 mg ml^{-1}). Different amount of $FeCl_2 \cdot 4H_2O$ was added into the GO suspension in a proper molar ratio, according to the oxygen-containing functional groups on GO surface. After ultrasonic dispersion for 1 h, ammonia was added in drops to adjust the pH value of the mixture. The pH value of the mixture was controlled at approximately 10. Then the whole suspension was transferred into a Teflon-lined stainless steel autoclave and reacted at 160^oC for 4 h. The black mixture was collected by centrifugation. After washing with adequate water and ethanol, the Fe_3O_4/graphene composites was finally obtained by drying in a vacuum oven at 80^oC for 24 h.

2.2 Characterization

The composites were characterized by powder X-ray diffraction (XRD) using a Rigaku D/Max-2550-PC X-ray diffractameter with Cu-K*a* irradiation (λ=0.15406 nm). The data were collected between scattering angles (2θ) of 10-90º at a scanning rate of 5º min^{-1}. The morphology and microstructure of the samples were observed using a transmission electron microscope (TEM, JEOL-2100F). TEM specimens were prepared by drop-casting the as-prepared sample dispersions onto carbon-coated TEM grids and dried in air. Thermogravimetric analysis (TGA) data were gathered using a Netzsch STA449C with a heating rate of 10^oC min^{-1} from room temperature to 850^oC to confirm the weight percent of Fe_3O_4 and graphene in the composites. The products were also characterized by a confocal microsphere Raman system (Labram-HR, France, 514.5 nm as excitation source and a spot size of 2 μm). The Si peak at 520 cm^{-1} was used as a reference to calibrate the wavenumber. X-ray photoelectron spectroscopy (XPS) data were taken on an AXIS Ultra instrument from Kratos Analytical in the range of 1-1300 eV to investigate the surface chemistries of the obtained materials.

2.3 Electrochemical measurements

The electrochemical properties of Fe_3O_4/graphene composites as anode materials of LIBs were evaluated at room temperature (25±1^oC). The test electrodes were prepared by mixing 80 wt.% active material with 10 wt.% acetylene black and 10 wt.% poly(vinylidene fluoride) (PVDF) dissolved in N-methyl-2-pyrrolidone (NMP) to form a homogeneous slurry, which was then uniformly coated onto the copper foil substrate with a blade. The as-prepared electrode sheets were placed in a vacuum oven at 120^oC to evaporate the solvent. Afterwards, the copper foil was punched into small disks with a diameter of 14 mm. The mass loading of the active materials was around 1.5 mg. The electrolyte used was 1 M $LiPF_6$ in a 1:1 weight ratio ethylene carbonate (EC):dimethyl carbonate (DMC) solvent. CR2032-type coin cells were fabricated in a glove box with an argon atmosphere. The Li metal foil was used as the counter electrode. Assembled cells were allowed to soak overnight before electrochemical testing. Electrochemical impedance spectroscopy (EIS) measurements were carried out in a two-electrode cell in the frequency range from 0.1 Hz to 100 kHz on a Princeton electrochemical workstation (M2273). Cyclic Voltammery (0.01-3 V, 0.1 mV s^{-1}) were performed on a CHI660D electrochemical workstation (Shanghai Chenhua Co. Ltd., China). Galvanostatic charge and discharge of the assembled cells were performed with a NEWARE battery tester at a voltage window of 0.01 and 3.0 V (*vs*. Li^+/Li).

3. RESULTS AND DISCUSSIONS

3.1 Formation of Fe_3O_4/graphene composites

The surface of GO single sheets prepared by the modified Hummer's method was covered with many oxygen-containing functional groups. The abundant functional groups (epoxy-, hydroxyl-, carboxyl-), presumed to be uniformly distributed on the surface of GO sheets, can act as anchoring sites for iron ions through electrostatic attraction. Therefore, we can assume that the oxygenated groups coordinate the iron ions and act as a nucleation center for the iron oxides growth. It enables the deposition of nanoparticles to uniformly distribute on graphene sheets through interaction with oxygen-containing functional groups. XPS was employed to analyze the chemical information of GO and the products of solvothermal reactions. Figure 1 shows the XPS spectra and C_{1s} spectra of as-prepared GO and solvothermal reaction products. The main signals presented on the survey spectra of GO were due to C and O, which were also the main components along with Fe in the iron oxides/graphene composites (fig.1a). The C_{1s} high-resolution XPS spectrum of GO (fig.1b) contained four typical components, corresponding to the carbon atoms in four types of functional group, the nonoxygenated ring C (285 eV, 39.36 at.%), the C in C-O bond (286.5 eV, 19.55 at.%), the C in carbonyl (288.6 eV, 29.87 at.%), and the C in carboxyl (290.2 eV, 11.22 at.%). This indicated that a fairly high degree of oxidation was carried out during the Hummers method. In this work, the anchoring amount of iron oxides was adjusted in direct proportion to the molar mass of oxygen-containing groups on GO surface in order to ensure the uniform distribution of iron oxides on the

surface of graphene sheets. The molar ratio of iron ions and oxygen-containing groups of GO was controlled in 3:1 and 3:2, respectively, which were abbreviated to S_1 and S_2, respectively.

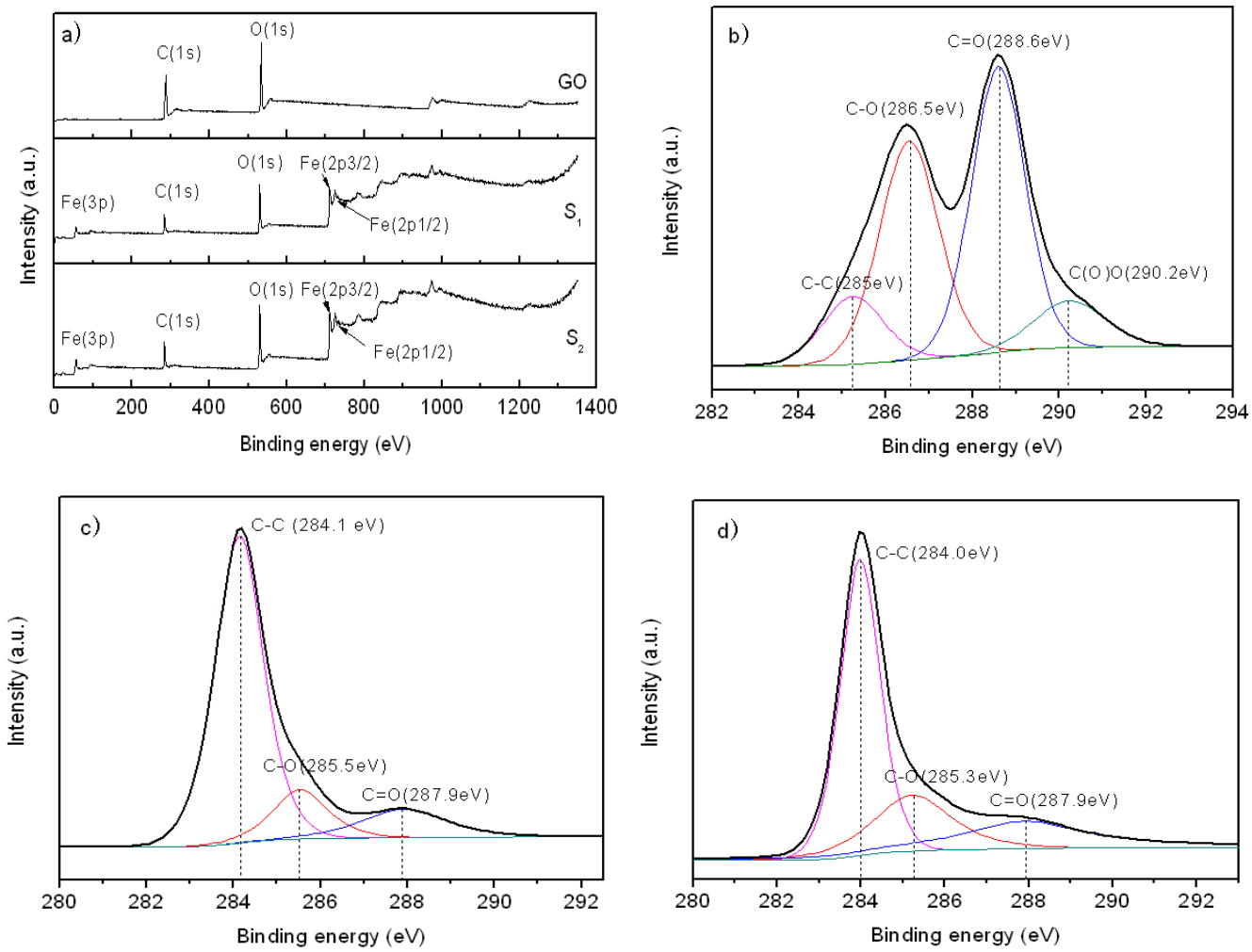

Figure 1. XPS spectra of GO and Fe_3O_4/graphene composites (a), and their C_{1s} spectra of GO (b), S_1 (c) and S_2 (d).

After solvothermal reaction, the relative intensities of those three components associated with oxygen-containing functional groups of GO in S_1 (fig.1c) and S_2 (fig.d) decreased markedly, specially, the O-C=O peak almost vanished, suggesting that most of the oxygen functional groups had been successfully removed. For the sample S_1, the carbon contents of C-O and C=O peaks were 7.72 at.% and 6.59 at.%, respectively, whereas, for the sample S_2, the carbon contents of C-O and C=O peaks were relatively lower, less than 60% that of S_1, 4.41 at% and 3.91 at.%, respectively. This abnormal phenomenon demonstrated that the amount of the residual oxygen-containing functional groups on graphene sheets didn't decrease with the increase of Fe(II) ions, suggesting that for the sample S_1, maybe due to the steric hindrance, ionic repulsion or the hindrance of the crystallization kinetics of Fe_3O_4, not all the oxygen-containing functional groups on GO could coordinate with Fe (II) ions.

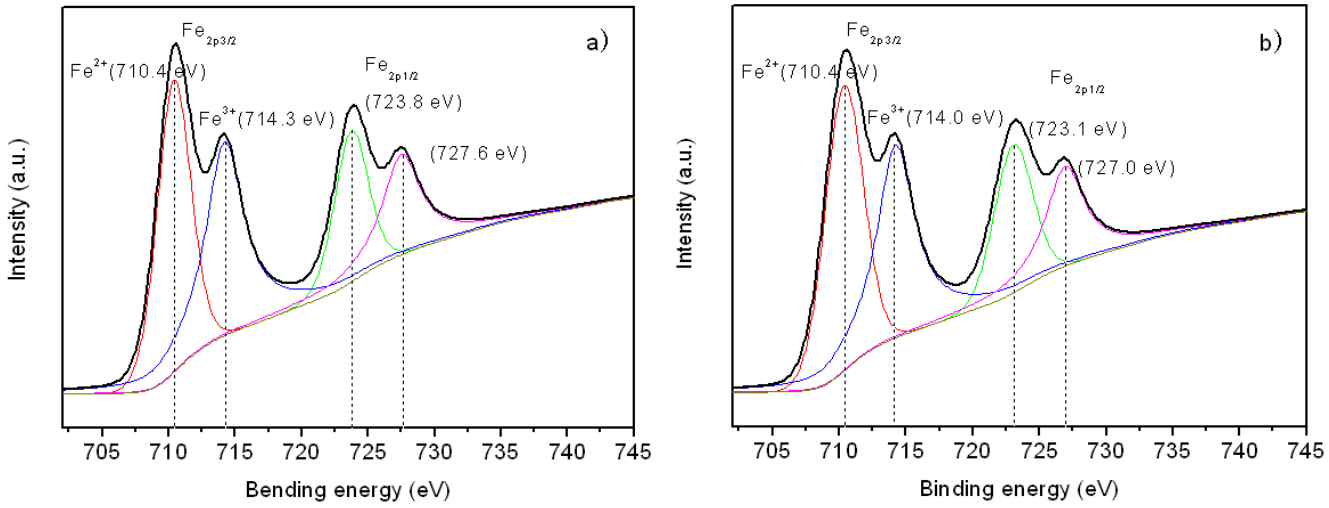

Figure 2. XPS spectra of Fe_{2p} of the sample S_1 (a) and S_2 (b).

Figure 2 presents the Fe_{2p} high-resolution XPS spectrum of S_1 (fig.2a) and S_2 (fig.2b). The binding energies of $Fe_{2p3/2}$ and $Fe_{2p1/2}$ were found at 710.1 eV and 725.3 eV, respectively, as shown in fig.1a. It is noteworthy that in both S_1 and S_2 samples, the peaks of $Fe_{2p1/2}$ were detected at about 723 eV and 727 eV, respectively, indicating the formation of mixed oxides of Fe (II) and Fe (III), such as Fe_3O_4 [21]. The peak of $Fe_{2p3/2}$ for S_1 and S_2 was composed of two peaks at about 710.4 eV and 714 eV, respectively, further confirming the formation of Fe_3O_4 [22]. In addition, the high-resolution O_{1s} XPS spectra (fig.3) of S_1 and S_2 were also studied in detail. Both the O_{1s} peak of S_1 (fig.3a) and S_2 (fig.3b) could be fitted to three peaks at 529.6 eV, 531.1 eV and 533 eV, respectively. The peak at 533 eV was attributed to the C-O group in graphene sheets, while the one at 529.6 eV was arisen from Fe_3O_4. The peak at 531.1 eV should be caused by the bond of Fe-O-C formed between Fe_3O_4 and graphene [23].

Table 1. The atomic percentages of the elements calculated by using sensitivity factors for Fe_3O_4/graphene composites

Atomic orbital	Peak position of S_1 (eV)	Compounds	Atomic concentration of each	Peak position of	Atomic concentration of each
C_{1s}	284.1	C-C	18.63	284.0	23.59
	285.5	C-O	7.27	285.2	4.41
	287.9	C=O	6.59	288.0	3.91
O_{1s}	529.6	Fe_3O_4	22.38	529.6	21.39
	531.0	Fe-O-C	7.59	531.1	10.19
	532.5	C-O	2.64	532.7	2.65
Fe_{2p}	710.4	Fe_3O_4	8.81	710.3	8.14
	723.7		8.92	723.1	8.24
	714.2		8.47	714.2	8.62
	727.5		8.71	727.0	8.87

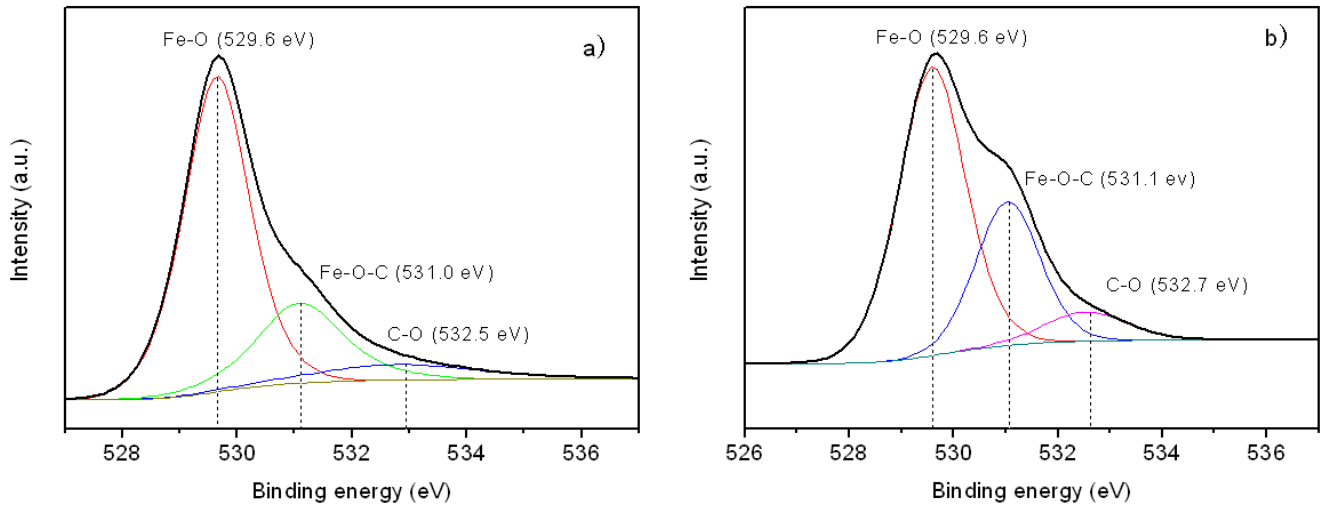

Figure 3. XPS spectra of O_{1s} of the sample S_1 (a) and S_2 (b).

Table 1 listed the atom composition of C_{1s}, O_{1s} and Fe_{2p} in Fe_3O_4/graphene composites through peak fitting. According to the peak fitting results, all the iron in the composite of S_2 existed in Fe_3O_4 and Fe-O-C, and there were only a few oxygen-containing functional groups of the residual C-O and C=O peaks remained. However, for sample S_1, there was a certain amount of Fe_3O_4 crystallizing outside graphene and indirectly contacting with it, which would result in a poor electric conductivity of S_1. The O-C=O peak cannot be detected by C_{1s} XPS spectra of Fe_3O_4/graphene composites, only a few C=O and C-O or C-OH groups were detected, suggesting the reduction of GO and presence of interfacial interaction (Fe-O-C linkage) between Fe_3O_4 nanoparticles and graphene. The Fe-O-C linkage between Fe_3O_4 nanoparticles and graphene nanosheets ensured the strong interfacial interaction and structure stability of Fe_3O_4/graphene composites.

3.2 Structure and morphology of Fe_3O_4/graphene composites

X-ray diffraction (XRD) patterns were used to investigate the phase and structure of GO and the Fe_3O_4/graphene composites (fig.4). The XRD pattern of GO exhibited a sharp peak at $2\theta=10.5^o$, indicating the characteristic (001) reflection, as shown in the inset figure of fig.4. Fe_3O_4/graphene composites displayed different XRD patterns from GO. The positions and relative intensities of the diffraction peaks matched well with the standard XRD data of Cubic Fe_3O_4 (JCPDS card No. 86-1359), while the characteristic diffraction peak of graphite located at 26.4^o couldn't be observed, revealing that Fe_3O_4 nanoparticles were efficiently deposited on the graphene surface, suppressing the stacking of graphene layers, and no graphite-like layered structure was formed by re-stacking of chemically reduced graphene in this condition [24]. Therefore, the diffraction peak of graphite disappeared in the XRD patterns of the sample S_1 and S_2. XRD observation confirmed the effective reduction of GO and the successful deposition of Fe_3O_4 nanoparticles on the surfaces of graphene sheets by the one-pot solvothermal reaction, which was consistent with the results of XPS analysis.

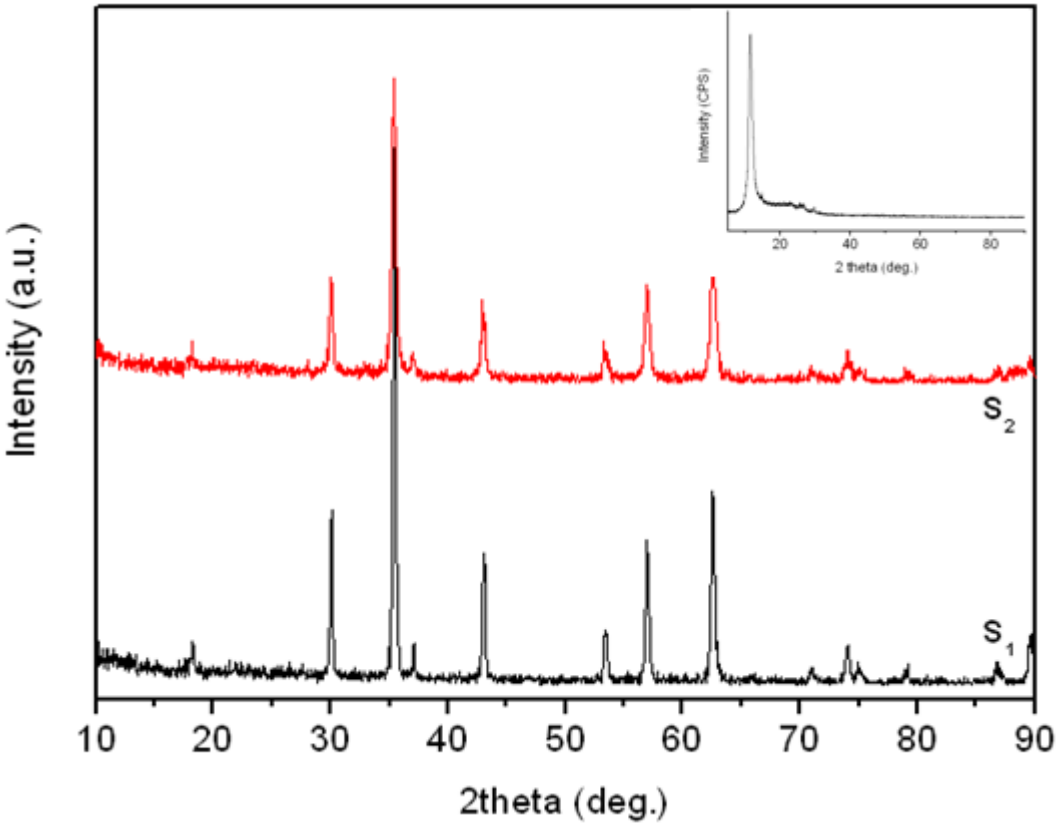

Figure 4. XRD patterns of Fe_3O_4/graphene composites, the inset figure is the XRD pattern of the original GO.

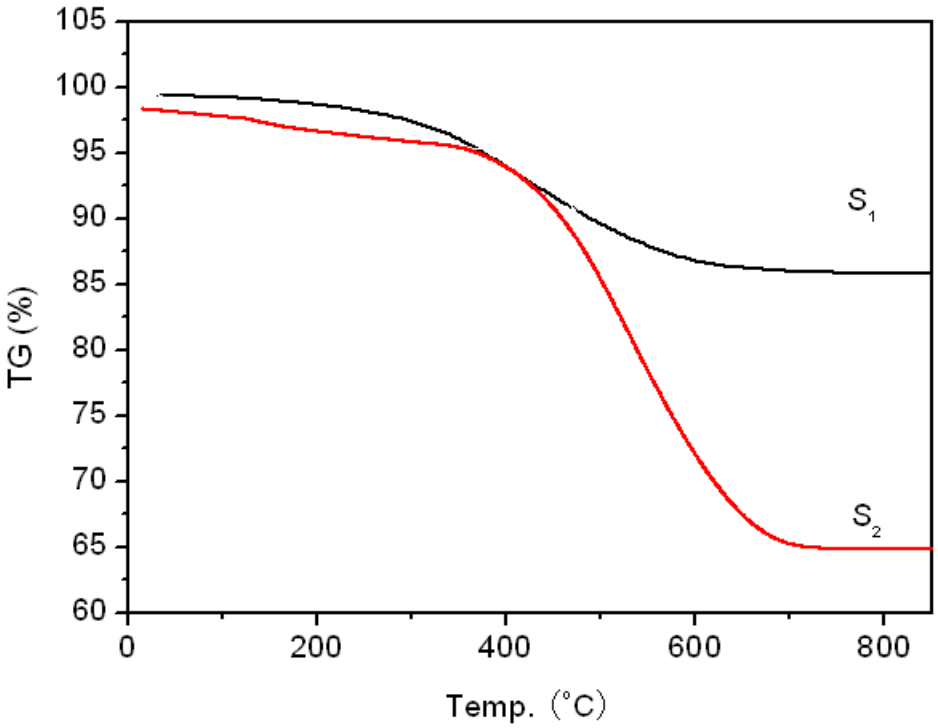

Figure 5. TGA curves of Fe_3O_4/graphene composites.

The weight ratio of graphene in Fe_3O_4/graphene composites was evaluated by the thermal gravimetric analysis (TGA) in air. The representative TG analysis curves of Fe_3O_4/graphene composites between room temperature and 850^oC are shown in fig.5. A slow mass loss observed between room temperature and 360^oC could be attributed to the removal of the remaining water and solvent in the first stage. In this stage, the total weight loss of the sample S_1 and S_2 was all approximately 5 wt.%, whereas the major weight losses occurred in the range of 360-700^oC, corresponding to the release of CO and CO_2. Assuming that the final residues are Fe_3O_4, the reduced weight may correspond to the oxidation of graphene nanosheets. According to the weight changes of the sample S_1 and S_2, the amount of graphene nanosheets in the sample S_1 and S_2 were 14.2 wt.% and 35.2 wt.%, respectively. Correspondingly, the anchoring amount of Fe_3O_4 in the sample S_1 and S_2 were 85.8 wt.% and 64.8 wt.%, respectively.

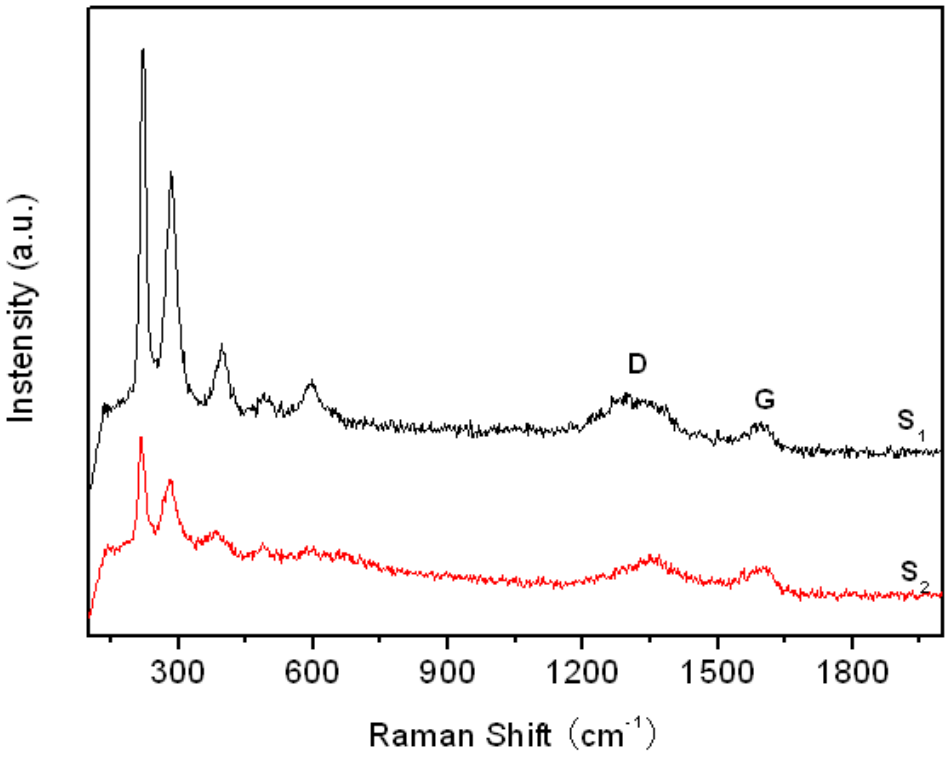

Figure 6. Raman spectra of Fe_3O_4/graphene composites.

Figure 6 shows the Raman spectra of Fe_3O_4/graphene composites. The Raman spectra of the composites had several typical peaks of the Fe-O stretching vibration, indicating that Fe_3O_4/graphene composites were successfully synthesized. The Raman bands at 218.8 and 491.3 cm^{-1} could be assigned to the scattering of A_{1g} mode of Fe_3O_4, while the bands at 283, 394.1 and 593.4 cm^{-1} were attributed to the scattering of E_g mode of Fe_3O_4. Besides, the intensity of the bands corresponding to Fe_3O_4 increased with the increase of the amount of Fe_3O_4 in the composites. The characteristic D and G bands for the composites were observed at 1344 and 1586 cm^{-1}, respectively. As we all known, the D band is associated with the disordered samples or graphene edges, while the G band is the result of

the first-order scattering of the E_{2g} mode of sp^2 carbon domains. Both the position and intensity of D and G bands are highly susceptible to the structural changes of the carbon matrix, and there are many factors which can affect the position and intensity of D and G bands, such as doping, layer numbers, defects, strains, substrates, etc [26]. The G bands (1586 cm^{-1}) of Fe_3O_4/graphene composites exhibited red shifts compared with those of pure graphene (1593 cm^{-1}), suggesting the n-type doping effect on grahene (electron donating effect) [25], and significant electronic interactions between graphene and Fe_3O_4. In addition, the ratio of I_D/I_G of S_1 was 4.82, nearly two-fold that of S_2 (I_D/I_G =2.42), also confirming a relatively larger amount of Fe_3O_4 doping in S_1 than in S_2.

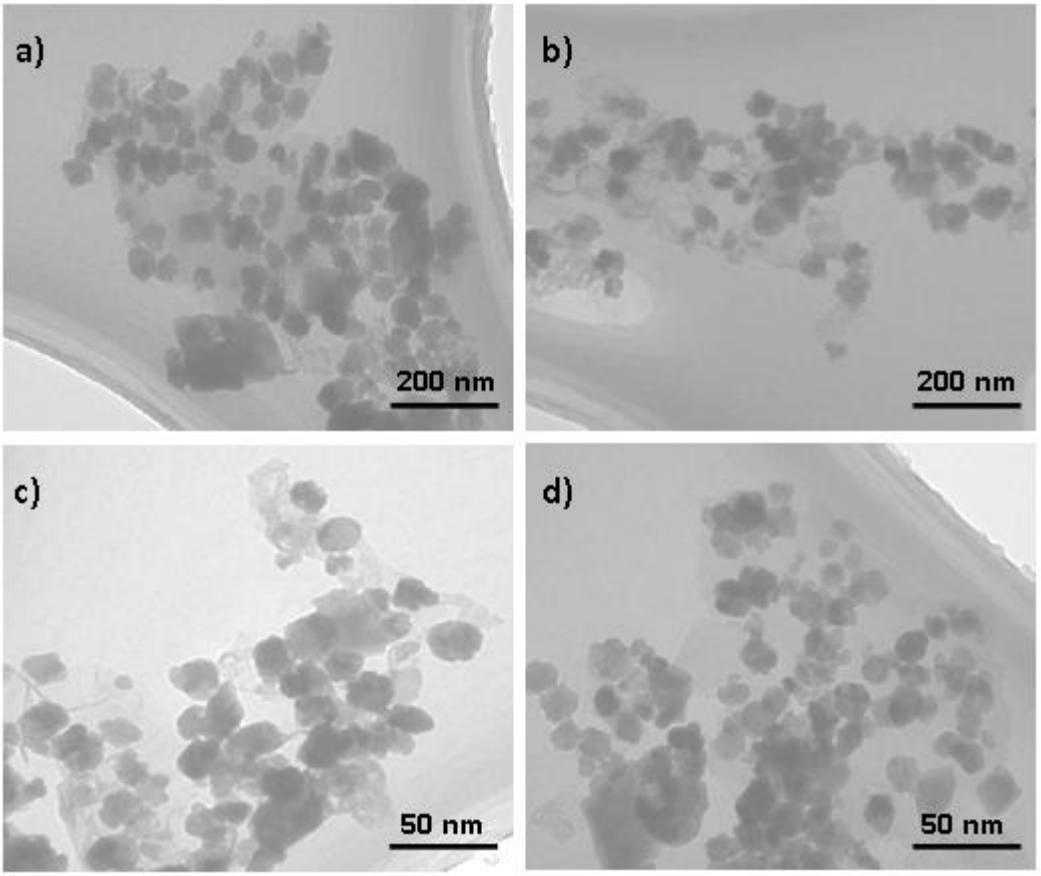

Figure 7. TEM images of Fe_3O_4/graphene composites: (a) low resolution images of S_1, (b) low resolution images of S_2, (c) high resolution image of S_1 and (d) high resolution image of S_2.

To further evaluate the morphology and structure of Fe_3O_4/graphene composites, TEM images are shown in fig.7a-d. They present the representative TEM images of Fe_3O_4/graphene composites prepared at the same reaction temperature and reaction time, while the molar ratio of the oxygen-containing functional groups of GO and Fe(II) ion was controlled in 1:3 and 2:3, respectively. According to the lower resolution images of S_1 (fig.7a) and S_2 (fig.7b), Fe_3O_4 nanoparticles uniformly dispersed on the surface of graphene sheets, and effectively prevented the aggregation of Fe_3O_4 nanoparticles and graphene restacking. Moreover, it clearly demonstrated that a relatively larger amount of Fe_3O_4 nanoparticles deposited on the surface of graphene of S_1. The higher resolution

observation of S_1 (fig.7c) and S_2 (fig.7d) revealed that with the decrease of Fe(II) ions concentration in the precursor mixture, the size and coverage density of Fe_3O_4 nanoparticles on graphene sheets were obviously decreased. Correspondingly, the surface of the graphene sheets was densely covered by spherical Fe_3O_4 nanoparticles with an average size of ~20 nm (S_1) and 15 nm (S_2), respectively. The distribution of magnetic particles was monodispersed and uniform. No obvious vacancy on graphene sheets was observed. Besides that, the graphene sheets remained flat, and no curled or crumpled sheets were observed, despite the high coverage of nanoparticles on the surfaces of graphene. However, a certain amount of agglomeration of Fe_3O_4 was observed in S_1, further confirming the XPS deduction. The appearance of this phenomena seems to be reasonable because with the increase of Fe(II) ions concentration in the precursor, more Fe_3O_4 would nucleate deviating from the oxygen-containing functional groups on the surface of graphene, resulting in the increase of the size and coverage density of Fe_3O_4 nanoparticles. Thus, there were slightly more residual oxygen-containing functional groups on the surface of graphene of S_1, as revealed by XPS analysis. In contrast, there was no obvious agglomeration of Fe_3O_4 observed in S_2, also consistent with the deduction of XPS.

3.3 Electrochemical properties of Fe_3O_4/graphene composite anodes

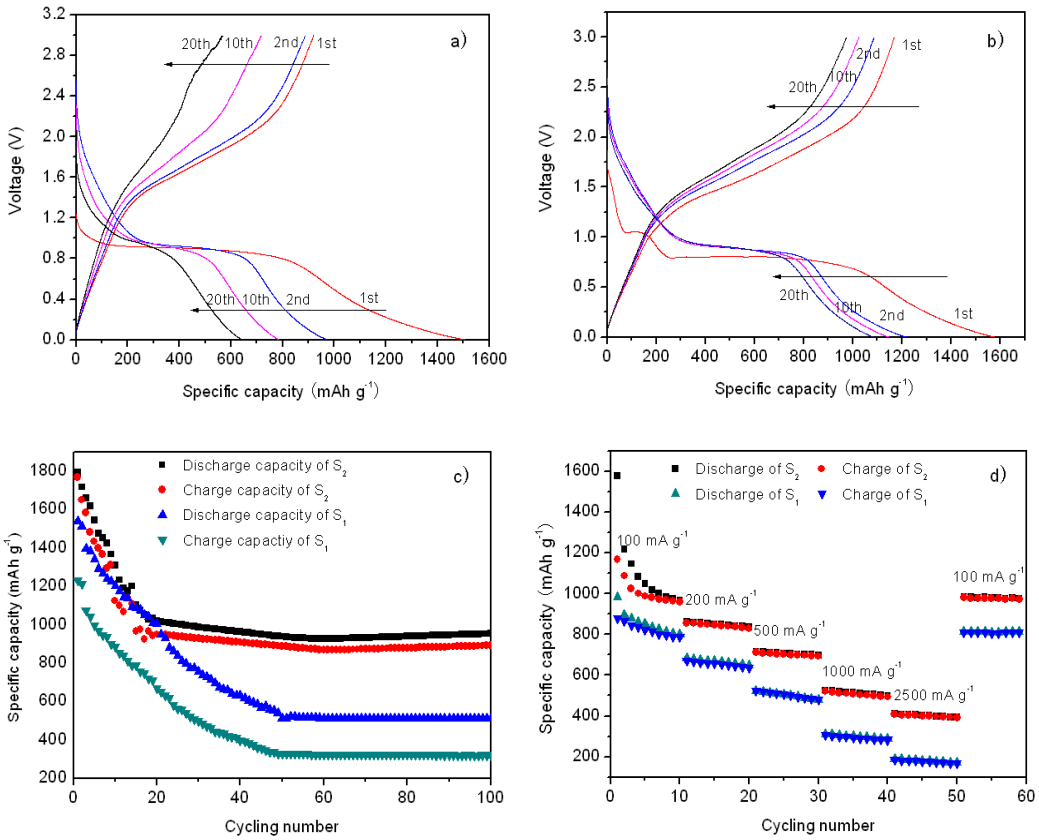

Figure 8. Discharge/charge curves of S_1 (a) and S_2 (b) at a current density of 100 mA g^{-1}, (c) cycling performance of S_1 and S_2 at a current density of 100 mA g^{-1} and (d) rate performance for Fe_3O_4/graphene composites.

Galvanostatic charge-discharge experiments were carried out to evaluate the electrochemical performance of as-prepared Fe_3O_4/graphene composites. The 1st, 2nd, 10th and 20th charge-discharge curves of the sample S_1 and S_2 under a current density of 100 mA g^{-1} are presented in fig.8a and b, respectively. The electrode based on S_1 delivered a discharge capacity of 1505 mAh g^{-1} and a charge capacity of 922 mAh g^{-1} at the 1st cycle with a coulombic efficiency of 61.26%. Comparatively, the electrode based on S_2 delivered a discharge capacity of 1572 mAh g^{-1} and a charge capacity of 1169 mAh g^{-1} with a coulombic efficiency of 74.36%. The coulombic efficiency of the composites rapidly increased to 90% in the 2nd cycle, and remained at more than this value in the following cycles. The discharge capacity of S_1, however, decreased greatly after 20 discharge-charge cycles, from 1505 to 635.4 mAh g^{-1}, decreased nearly 58%, while the discharge capacity of S_2 decreased slightly, less than 32%.

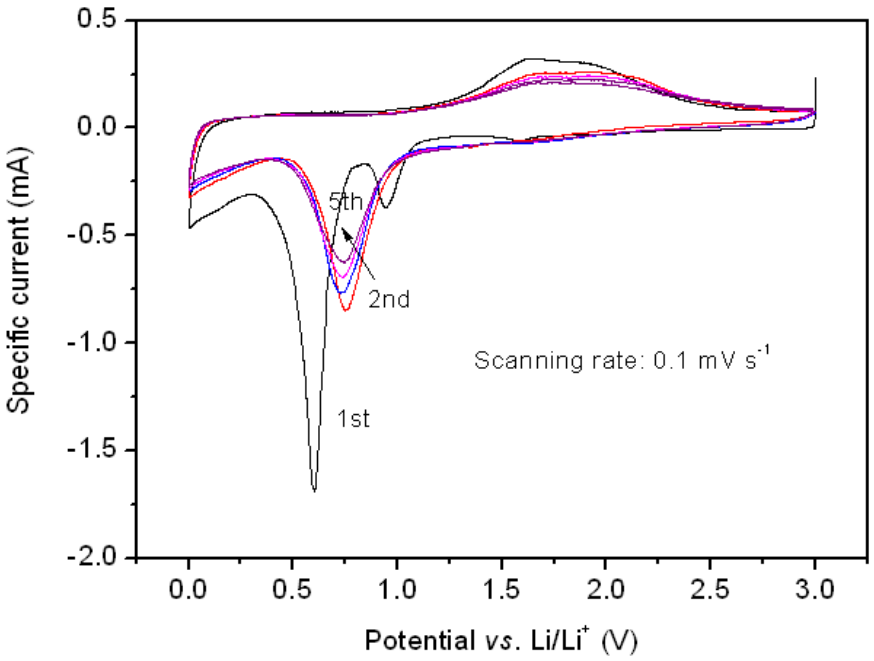

Figure 9. Cyclic voltammograms (CV) of the sample S_2 in the voltage range of 0-3.0 V at a scanning rate of 0.1 mV s^{-1}.

Figure 8c shows the cyclic performances of S_1 and S_2 at a current density of 100 mAh g^{-1}. The discharge-charge performance of S_2 decreased steadily in the first 20th cycles, and then decreased slightly. Since the 60th cycle, the discharge and charge capacities of S_2 began to increase gradually. After 100 discharge-charge cycles, the charge and discharge capacity were 891 and 953 mAh g^{-1}, respectively. The enhanced cyclic performance of S_2 could be ascribed to the gradual activation of Fe_3O_4/graphene composites in the initial stage [27]. Compared with S_2, the discharge-charge capacity of S_1 decreased greatly in the first 50th cycles, and then remained steady. After 100 discharge-charge cycles, S_1 exhibited a lower discharge and charge capacity of 516.7 and 322.7 mAh g^{-1}, respectively, maybe due to the aggregation of large-size Fe_3O_4 particles.

The rate performance of Fe_3O_4/graphene composites is presented in fig.8d. S_2 exhibited a superior rate capacity than S_1 at various current densities from 100 to 2500 mA g^{-1}. The reversible capacity of Fe_3O_4/graphene composites decreased slightly in the first 10 cycles at a current density of 100 mA g^{-1}. In the following cycles, S_2 kept a reversible capacity of 974, 835, 701, 497 and 393 mAh g^{-1} at the current density of 100, 200, 500, 1000 and 2500 mA g^{-1}, respectively. While S_1 showed a relatively lower reversible capacity of 810, 788, 636, 480, 281 and 168 mAh g^{-1} at the current density of 100, 200, 500, 1000 and 2500 mA g^{-1}, respectively. The specific capacity of S_2 at 2500 mA g^{-1} was 40.3% that of S_2 at 100 mA g^{-1}, whereas, the specific capacity of S_1 at 2500 mA g^{-1} remained only 20.7% of that at 100 mA g^{-1}. Furthermore, due to the gradual activation of graphene in the composites during the cycling processes, the obtained Fe_3O_4/graphene composites recovered to their original capacity or even a bit higher when the rate came back to the initial 100 mA g^{-1} after 50 cycles. The reversible capacity of S_2 could be fully recovered to 979 mAh g^{-1} at 100 mA g^{-1}.

Cyclic voltammetry (CV) measurements of Fe_3O_4/graphene composites of S_2 were carried out in the voltage range of 0-3.0 V *vs*. Li^+/Li at a scanning rate of 0.1 mV s^{-1} (fig.9). In the first cycle, two observed cathodic peaks at 0.6 V and 0.94 V could be attributed to the reduction of Fe^{3+} and Fe^{2+} to Fe^0 and the irreversible reaction related to the decomposition of electrolyte [28]. In this step, the conversion of Fe_3O_4 to Fe and the formation of Li_2O were the main reasons for the irreversible capacity loss during the discharge process. The broad anodic peak at about 1.6 V was corresponding to the irreversible oxidation of Fe^0 to Fe^{2+} and Fe^0 to Fe^{3+} during the charge process [29]. In the subsequent cycles, due to the hysteresis in the CV technique, the cathodic peak negatively shifted to approximately 0.7 V, while the anodic peak positively shifted compared to the discharge/charge voltage plateaus. But the peak intensity of CV curves and the integral area tended to be stable, which was consistent with the results of galvanostatic charge and discharge.

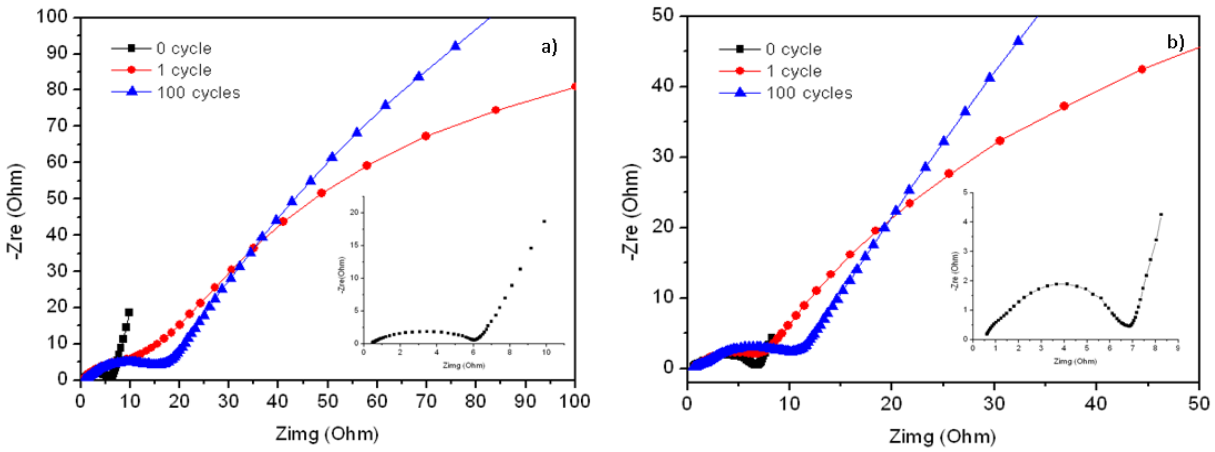

Figure 10. Nyquist plot of AC impedance spectra for Fe_3O_4/graphene composites: (a) S_1 electrode and (b) S_2 electrode. The inset figure in (a) and (b) is the Nyquist plot of S_1 and S_2 without suffering from charge and discharge cycle, respectively.

For the LIBs, the charge transfer resistance is a measure of the charge transfer kinetics, and the charge-transfer process determines the rate of transfer reaction. In order to gain an in-depth

understanding of the advantages of Fe_3O_4/graphene composite electrodes and the role of graphene, electrochemical impedance spectroscopy (EIS) was employed to investigate the electrochemical reaction kinetics of different electrodes (fig.10). The semicircle appearing in the medium frequency range is classically assigned to the charge-transfer resistance (R_{ct}) occurring between active materials and liquid electrolyte. The straight line is attributed to the diffusion of lithium ions into electrode materials or so-called Warburg diffusion. For the sample S_1 (fig.10a), R_{ct} was 5.6 Ω before cycling and increased dramatically to 10.6 and 15.7 Ω after 1 and 100 cycles (ΔR_{ct}=10.1 Ω), respectively. R_{ct} increased 1.8 fold after 100 cycles, suggesting a considerable degradation of charge transfer kinetics. This may be due to the severe pulverization of Fe_3O_4 and loss of electric contact with the current collector. In general, anode materials with higher specific capacity tend to undergo considerable amount of volume dilation between Li^+ inserted and exacted status. For Fe_3O_4 based anodes, the active materials transform from an oxide to metallic iron, such volume changes would result in pulverization of the active materials, disintegration of the anode assembly, poor cycling performance and capacity fade over several charge-discharge cycles [30]. Additionally, the particle size plays a drastic role on this process. Larger particles undergo an irreversible phase transformation, while smaller particles can reversibly and topotactically react with Li without phase transformation [31]. Although the particle size of Fe_3O_4 in S_1 was similar to that in S_2, the agglomeration of Fe_3O_4 in S_1 made it present the same characteristics as that of the larger size particles. While for the sample S_2 (fig.10b), ΔR_{ct} was only 3.4 Ω after 100 cycles, less than 33.7% of that of S_1 electrode, which was in good agreement with results of the cycle performance and rate capability, demonstrating that S_2 had formed a good conductivity network between Fe_3O_4 nanoparticles and graphene, and the degradation of charge transfer kinetics was greatly suppressed. Therefore, in this case, the improved electrochemical performance of the sample S_2 could be resulted from the small-sized Fe_3O_4 nanoparticles with high dispersion on graphene nanosheets, and the important interfacial interaction (Fe-O-C linkage) between Fe_3O_4 nanoparticles and ultrathin graphene nanosheets.

4. CONCLUSIONS

A novel one-step simple and environmentally friendly hydrothermal approach was applied to synthesize Fe_3O_4/graphene nanocomposites. The Fe_3O_4/graphene nanocomposite with excellent electrochemical properties has been successfully and directly prepared with a controlled Fe_3O_4 anchoring amount. The surface of reduced graphene oxide was homogeneously covered by spherical Fe_3O_4 nanoparticles with an average size of 15 nm. The optimized Fe_3O_4/graphene nanocomposite with well-designed structure exhibited remarkable lithium storage properties including high reversible capacity, excellent cycle performance and good rate capability. The superior performance could be attributed to the excellent mixed conducting networks, the stable microstructure of nanoparticles, and the flexible graphene matrix. In addition, the strong interfacial interaction between Fe_3O_4 nanoparticles and graphene matrix through Fe-O-C bonds further enhanced the electrical performance of Fe_3O_4/graphene composites and promoted the synergetic effects of Fe_3O_4 and graphene in the composites.

ACKNOWLEDGMENTS
This work was supported by the national science and technology support program of China (Grant No. 2013BAE04B03), startup fund for advance talent (Grant No. 11-08), education department of Heilongjiang province (Grant No.12521465) and science & technology innovation fund from Harbin administration of science & technology (Grant No. RC2012LX018001).

References

1. C.K. Tarascon and M. Armand, *Nature*, 44 (2001) 359.
2. C.K. Chan, H. Peng, G. Liu, K. McIlwrath and Y. Cui, *Nat. Nanotechnol*., 3 (2008) 31.
3. P. Lian, S. Liang, X. Zhu, W. Yang and H. Wang, *Electrochim. Acta*, 58 (2011) 81.
4. T.F. Yi, H.P. Liu, Y.R. Zhu, L.J. Jiang, Y. Xie and R.S. Zhu, *J. Power Sources*, 215 (2012) 258.
5. K.S. Novoselov, A.K. Geim, S.V. Morozov, D. Jiang, Y. Zhang and S.V. Dubonos, *Science*, 306 (2004) 666.
6. D.Y. Wei, J.G. Yu, H. Huang, Y.N. Zhuo and F.Q. Wang, *Mater. Lett*., 66 (2012) 150.
7. G. Williams, B. Seger and P.V. Kamat, *ACS Nano*, 2 (2008) 1487.
8. C.N.R. Rao, K. Biswas, K.S. Subrahmangama and A. Govindaraj, *J. Mater. Chem*., 19 (2009) 2457.
9. C.J. Fu, G.G. Zhao, H.J. Zhang and L. Shuang, *Int. J. Electrochem. Sci.*, 8 (2013) 6269.
10. P. Poizot, S. Laruelle, S. Grugeon, L. Dupont and J.M. Tarascon, *Nature*, 407 (2000) 496.
11. I. Bouessay, A. Rougier and J.M. Tarascon, *J. Electrochem. Soc*., 151 (2004) H145.
12. X.R. Wang, S.M. Tabakman and H.J. Dai, *J. Am. Chem. Soc*., 130 (2008) 8152.
13. I.R.M. Kottegoda, N. Hayati Idris, L. Liu, J.I. Wang and H.K. Liu, *Electrochim. Acta*, 56 (2011) 5815.
14. Y.S. He, D.W. Bai, X.W. Yang, J. Chen, X.Z. Liao and Z.F. Ma, *Electrochem. Commun*., 12 (2010) 570.
15. R.S. Ruoff, Y.W. Zhu, S. Murali, M.D. Stoller, K.J. Ganesh, W.W. Cai, P.J. Ferreira, A. Pirkle, R.M. Wallace, K.A. Cychosz, M. Thommes, D. Su and E.A. Stach, *Science*, 332 (2011) 1537.
16. Z.Y. Wang, D.Y. Luan, S. Madhavi, C.M. Li and X.W. Lou, *Chem. Commun*., 47 (2011) 8061.
17. V. Chandra, J. Park, Y. Chun, J.W. Lee, I.C. Hwang and K.S. Kim, *ACS Nano*, 4 (2010) 3979.
18. B.J. Li, H.Q. Cao, J. Shao, M.Z. Qu and J.H. Warner, *J. Mater. Chem*., 21 (2011) 5069.
19. X.Y. Wang, X.F. Zhou, K. Yao, J.G. Zhang and Z.P. Liu, *Carbon*, 49 (2011) 133.
20. X.D. Huang, X.F. Zhou, K. Qian, D.Y. Zhao, Z.P. Liu and C.Z. Yu, *J. Alloys Compd*., 54 (2012) 76.
21. J.S. Zhou, H.H. Song, L.L. Ma and X.H. Chen, *RCS Adv*., 1 (2011) 782.
22. P.C. Graat and M.A.J. Somers, *Appl. Surf. Sci*., 100/101 (1996) 36.
23. C. Combellas, M. Delamar, F. Kanoufi, J. Pinson and F.I. Podvorica, *Chem. Mater*., 17 (2005) 3968.
24. P.C. Lian, X.F. Zhu, H.F. Xiang, Z. Li, W.S. Yang and H.H. Wang, *Electrochim. Acta*, 56 (2010) 834.
25. W. Chan, S. Li, C. Chen and L. Yan, *Adv. Mater*., 23 (2011) 5679.
26. S. Pisana, M. Lazzeric, C. Casiraghi, K.S. Novoselov, A.K. Geim, A.C. Ferrari and F. Mauri, *Nat. Mater*., 6 (2007) 198.
27. S.K. Behera, *Chem. Commun.*, 47 (2011) 10371.
28. S.L. Jin, H.G. Deng, D.H. Long, X.J. Liu, L.A. Zhan, X.Y. Liang, W.M. Qiao and L.C. Ling, *J. Power Sources*, 196 (2011) 3887.
29. Y. Chan, H. Xia, L. Lu and J. Xue, *J. Mater. Chem*., 22 (2012) 5006.
30. Y. Idota, T. Kubota, A. Matsufuji, Y. Miyasaka, *Science*, 276 (1997) 1395.
31. D. Larcher, C. Masqnelier, D. Bonnin, Y. Chabre, V. Masson, J.B. Lariche, J.M. Tarascon, *J. Electrochem. Soc.*, 150 (2003) A133.

© 2014 by ESG (www.electrochemsci.org)